Research Article

Phase formation mechanism of Cr$_2$AlC MAX phase coating: *In-situ* TEM characterization and atomic-scale calculations

Guanshui Ma [a,1], Haichen Wu [b,1], Zhi Fang [c], Xiaohui Zhou [a], Rende Chen [a], Wei Yang [a], Jiayue Zhang [a], Zhenyu Wang [a,*], Aiying Wang [a,*]

[a] *Key Laboratory of Advanced Marine Materials, Ningbo Institute of Materials Technology and Engineering, Chinese Academy of Sciences, Ningbo 315201, China*
[b] *Analytical Center, Ningbo Institute of Materials Technology and Engineering, Chinese Academy of Sciences, Ningbo 315201, China*
[c] *Beijing Innovation Centre for Engineering Science and Advanced Technology, School of Materials Science and Engineering, Peking University, Beijing 100871, China*

A B S T R A C T

Cr$_2$AlC, a representative MAX phase, gains increasing attention for the excellent oxidation tolerance and corrosion resistance used in harsh high temperature and strong radiation environments. However, the lack of the phase formation mechanism has become the key bottleneck to the practical applications for Cr$_2$AlC synthesis with high purity at low temperatures. In this work, we fabricated the amorphous Cr–Al–C coating by a hybrid magnetron sputtering/cathodic arc deposition technique, in which the *in-situ* heating transmission electron microscopy (TEM) was conducted in a temperature range of 25–650 °C to address the real-time phase transformation for Cr$_2$AlC coating. The results demonstrated that increasing the temperature from 25 to 370 °C led to the structural transformation from amorphous Cr–Al–C to the crystalline Cr$_2$Al interphases. However, the high-purity Cr$_2$AlC MAX phase was distinctly formed at 500 °C, accompanied by the diminished amorphous feature. With the further increase of temperature to 650 °C, the decomposition of Cr$_2$AlC to Cr$_7$C$_3$ impurities was observed. Similar phase evolution was also evidenced by the Ab-initio molecular dynamics calculations, where the bond energy of Cr–Cr, Cr–Al, and Cr–C played the key role in the formed crystalline stability during the heating process. The observations not only provide fundamental insight into the phase formation mechanism for high-purity Cr$_2$AlC coatings but also offer a promising strategy to manipulate the advanced MAX phase materials with high tolerance to high-temperature oxidation and heavy ion radiations.

© 2024 Published by Elsevier Ltd on behalf of The editorial office of Journal of Materials Science & Technology.

1. Introduction

The MAX phases were first defined and renaissance developed by Barsoum et al. [1] in the early stage of 2000 as a new family of ternary nanolaminate ceramics, including carbides, borides, or nitrides, with a hexagonal close-packed (HCP) crystal structure [2,3]. Up to now, it is well established for the general formula of MAX or M$_{n+1}$AX$_n$ phase, where M stands for an early transition metal element, A presents an element from IIIA or IVA, and X is assigned to C, B, or N [4,5]. Depending on the value of n, MAX phases can be classified into 211 phases, 312 phases, 413 phases as well as even high-order MAX phases [6–9]. The crystal struc-

ture of the MAX phase is mainly composed of edge-shared M$_6$X octahedra, with M$_{n+1}$X$_n$ and A layers stacked alternately along the *c*-axis, resulting in strong M–X bonds and relatively weak M–A bonds, respectively [10,11]. Benefiting from the unique layered structure and atomic bond characteristics, MAX phases possess a combination of ceramic and metallic properties, such as outstanding damage tolerance [12–15], excellent corrosion/oxidation resistance [16,17], and high electrical conductivity [18,19]. These superior advantages enable the potential applications of MAX phases as protective coatings for vital components utilized in severe environments, such as advanced nuclear materials [20,21], solid lubricant materials [22,23], and aero-engine functional materials [24].

Among the MAX phase categories, Cr$_2$AlC is a typical representative of the 211 MAX phases, widely used as protective coatings with excellent oxidation and corrosion against high-temperature and heavy flux of ion radiations [25–27]. Moreover, the thermal expansion coefficient of Cr$_2$AlC (12~13 × 10^{-6} °C^{-1}) in the range of

---

30–1200 °C is similar to those of common metals most like stainless steel (SS) and Ni-based alloys [28]. Such merits not only benefit strong adhesion between Cr_2AlC coating and substrate but also contribute to the cracking/spallation resistance of Cr_2AlC coating during the post-annealing process, making the Cr_2AlC MAX phase increasingly popular [29]. Many reports have indicated that the physiochemical properties of Cr_2AlC MAX phase coatings are predominated by the crystalline state and phase purity in the band structure. For example, Zhang et al. [30] revealed that compared to the partially and fully crystalline Cr_2AlC MAX phase coating, the as-deposited amorphous Cr–Al–C coating exhibited the best corrosion resistance in 3.5 wt.% NaCl solution. Based on our previous work [31], a similar observation was that the partially crystallized Cr_2AlC coating possessed a superior performance in balancing corrosion current density and interfacial contact resistance than both the highly crystalline MAX phase and as-deposited amorphous coating in 0.5 M H_2SO_4 + 5 ppm HF solution. However, the reaction sequence of the phase formation for Cr_2AlC has not be clearly identified yet, due to the bonding diversity and structural complexity in MAX phases. Therefore, it has become a crucial and imperative challenge to control the crystalline phase characteristics of Cr_2AlC coating and thus facilitate the combinatorial performance required for the wide applications with various electrical, mechanical and electrochemical properties.

Taking the simplicity of bulk materials over coatings, Lin and co-authors [32] developed a synthesis route of bulk Cr_2AlC through hot pressing/solid-liquid reaction. They found that the thermal explosion reaction at 700 °C produced a significant amount of Cr–Al intermetallics, but the formation of the Cr_2AlC MAX phase only occurred at 1050 °C due to the reactions of intermediate products. The crystallization kinetics of sputtered amorphous Cr_2AlC powder implied a two-step process probably [33]. With a heating rate of 10 °C min^{-1}, the formation of a hexagonal $(Cr, Al)_2C_x$ solid solution was first evolved at around 560 °C, subsequently followed by the emergence of the Cr_2AlC MAX phase at 610 °C. In this aspect, the synthesis temperature for Cr_2AlC MAX phase coating was significantly reduced than that of bulk materials. Parallel observation was also reported in the Cr_2AlC thin film [34], where the phase crystallization appeared at 620 °C. In addition, using *ex-situ* X-ray diffraction (XRD), two exothermic reactions were addressed for the microstructure evolution from amorphous Cr–Al–C coating to Cr_2AlC MAX phase coating after the heating process, where the hexagonal $(Cr, Al)_2C_x$ was predominated at an onset temperature of 570 °C but the crystalline Cr_2AlC came out at 660 °C.

Different from the *ex-situ* characterization, in recent years, various *in-situ* testing technologies, such as *in-situ* resistivity [35], *in-situ* XRD [36], and *in-situ* transmission electron microscopy (TEM) [37–39], have been employed to investigate the phase changes and microstructural evolution in MAX phase coatings and relevant multi-component coatings. Particularly, utilizing *in-situ* heating XRD analysis, we have recently reported the dependence of the MAX phase evolution in as-deposited M–Al–C (M = Ti, V, Cr) coatings on the heating temperatures [24], where the Ti_2AlC coating clearly displayed a higher phase-forming temperature accompanied with a lack of any intermediate impurities comparing with V_2AlC and Cr_2AlC cases. The reason behind this phenomenon could be due to the larger formation energy and density of states in the Ti_2AlC system than the other two coatings based on the combined theoretic simulations. However, considering the existence of complicated bonds in MAX phases, the diversity in synthesis techniques, and limited atomic resolution in the XRD technique, the *in-situ* heating TEM approach would be the best strategy to further identify the real-time characterization of evolving the chemical reactions, subtle structural changes, crystalline phase transformations, and events like nucleation or void nullification. Nevertheless, to the best of our knowledge, no available studies have yet

been attempted for phase formation and microstructure evolution in Cr_2AlC MAX phase coatings by *in-situ* heating TEM.

In the present work, our ambition was to shed light on the phase formation mechanism of Cr_2AlC MAX phase coating from the as-deposited amorphous Cr–Al–C case in terms of the microstructural characterization and crystalline growth by an *in-situ* heating TEM technique. In particular, the testing temperature was *in-situ* controlled from 25 to 650 °C at a heating rate of 10 °C min^{-1}. Furthermore, the dependence of microstructural characterization on the atomic-scale band states was also comparatively investigated by the Ab-initio molecular dynamic calculations based on the density-functional theory (DFT).

2. Experimental process

### 2.1. Preparation of Cr–Al–C coatings

The Cr–Al–C coatings were prepared by the same method described in our previous report [31]. SS316L with dimensions of Φ 15 mm $\times$ 3 mm was employed as the substrate, and the composition was the same as that used in our previous work [28]. To remove surface contaminants and improve adhesion strength, all the SS316L substrates were polished using a diamond paste polisher (No. 5) and washed sequentially with acetone and alcohol before being put into the evacuated chamber. Fig. 1(a) shows the hybrid cathodic vacuum arc combined with a direct current (DC) magnetron sputtering deposition system for the synthesis of Cr–Al–C coatings. Specifically, Al target and Cr target with the purity of 99.9 % were used as the sputtering source and arc source, respectively. The basic pressure of chamber was maintained at 3 $\times$ 10^{-5} Pa, and the substrate was supplied with the DC bias of –150 V. The substrate holder was rotated throughout the deposition process, where the distance between the substrates and targets was set at 80 mm. The pristine Cr–Al–C coatings were deposited by arc-discharged Cr and sputtered Al targets at a power level of 0.9 and 2.8 kW, respectively, accompanied by an introduction of Ar and CH_4 flow rates of 200 and 30 sccm to the chamber. The deposition time lasted for 150 min and no extra heating was applied for all the deposition. More details about the preparation procedure could be referred to our previous works [31].

2.2. Preparation and heating of TEM sample

The TEM specimen was facilitated using a FEI Helos G4 CX focused ion beam (FIB). The sample was fixed on a specifically machined micro-heater chip, as depicted in Fig. 1(b). Prior to FIB preparation, the existence of SiN film on the chip was removed, and the sample was directly bonded to the film-free hole. The *in-situ* heated experiment was carried out using a Nano-Ex FEI MEMS heating holder. The sample was gradually heated from room temperature ($\sim$25 °C) to 500 °C at a rate of 10 °C min^{-1}, then maintained at 500 °C for 30 min to ensure temperature uniformity distributed in the coatings, followed by further heated to 650 °C also at a rate of 10 °C min^{-1}. The *in-situ* microstructure characterization was performed using a Talos F200X TEM with an acceleration voltage of 200 kV and equipped with four energy-dispersive X-ray spectroscopy (EDS) detectors.

2.3. Computational details

The structural optimizations, bond lengths and binding energies were calculated by first-principles calculations based on DFT with the specialized Vienna Ab-initio Simulation Package (VASP). The exchange-correlation energy was evaluated using the Perdew-Burke-Ernzerhof functional within the generalized gradient
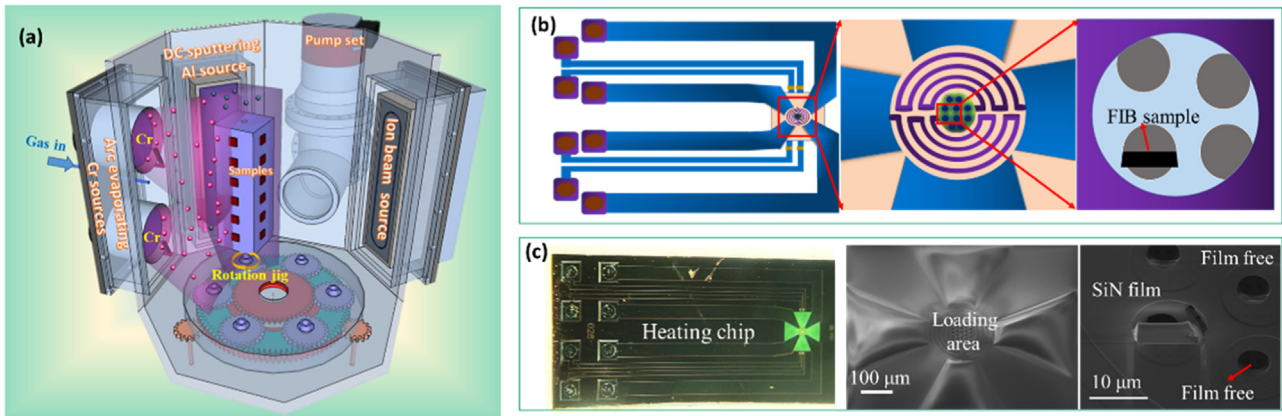
Fig. 1. (a) A schematic of hybrid cathodic arc/magnetron sputtering for depositing of Cr–Al–C coatings. (b) Schematic diagram and (c) the corresponding images of *in-situ* heating TEM treatment for Cr–Al–C coating.

approximation [40,41]. The electron-nucleus interaction was described by the projector augmented wave (PAW) method, together with a plane-wave energy cutoff of 500 eV [42]. The valence electron configurations of Cr, Al, and C were $3p^63d^54s^1$, $3s^23p^1$, and $2s^23p^2$, respectively. All structures were optimized with a convergence criterion of 1.0×10^{-5} eV for the energy and 0.05 eV Å^{-1} for the forces. The strong correlation in the 3d orbitals of Cr atoms is treated by the GGA + U method including an on-site Coulomb interaction of U = 4.08 eV [43].

In order to address the real-time evolution in the phase structure, Ab-initio molecular dynamics (AIMD) simulations were further conducted for Cr_2Al and Cr_2AlC slabs using on-the-fly machine learning force fields. The simulations were performed in a canonical ensemble, utilizing a Nosé-Hoover thermostat (NVT) [44]. The PAW method and PBE functional implemented in VASP were used as well. The temperature was set at 500 °C with a time step of 1 fs. A simulation time of 10 ps was required to allow the energy and structure of the system to reach equilibrium, as previously reported in the literature [45–48]. The other basic parameters were consistent with those used in the common DFT calculations.

3. Results and discussion

The TEM sample was mounted onto a micro-heater chip with a size of 6 μm × 3 μm in length and width. Fig. 2 shows the microstructure and elemental distribution for the as-deposited Cr–Al–C coating sample. It was obvious that a homogeneous structure without any porosity or void defects was obtained from the selected bright field image in the as-deposited sample before the *in-situ* heating measurement (Fig. 2(a)). According to the high-resolution TEM (HRTEM) image and selected area electron diffraction (SAED) image in Fig. 2(b, c), there was a lack of apparent lattice fringes despite the existence of hallo diffuse rings [31]. The observation evidenced the amorphous microstructure for the as-deposited Cr–Al–C coating. The high-angle annular dark field (HAADF) image deduced from scanning transmission electron microscopy (STEM) was further shown in Fig. 2(d), where a fine periodic structure with alternating bright and dark layers was revealed in a nano-scaled dimension from the pristine coating. The nanolaminate structure with distinct contrast across the coating thickness was primarily attributed to the different concentrations of Cr and Al elements, as discussed in our previous report [49]. The elemental mappings consisting of the distributed compositions were indicated in Fig. 2(e–g). The distribution of the C atom was relatively uniform, while the Cr and Al cases exhibited the alternated distribution with period modulation. Additionally, the con-

stituents determined by EDS were approximately Cr: 50.36 at.%, Al: 28.15 at.%, and C: 21.49 at.% (Fig. 2(h)), implying the stoichiometry of Cr: Al: C near 2:1:1. Therefore, it could be said that the as-deposited Cr–Al–C coating possessed the remarkable homogeneous and typical amorphous structure with a stoichiometry close to the ideal Cr_2AlC MAX phase.

To investigate the phase evolution of Cr–Al–C coating relevant to temperature, the sample was gradually heated from room temperature to 650 °C, with corresponding TEM bright field images provided in Fig. 3. Until the temperature reached 230 °C, no obvious changes in the amorphous structure could be distinguished. However, noted that at this temperature, particles with black contrast (indicated by the red arrow in Fig. 4(a)) first appeared in the nano-scale layered structure. The HRTEM image (Fig. 4(b)) revealed that such black particles existed in well nanocrystalline characteristics. If one kept in mind of the difference between *in-situ* and *ex-situ* microstructure characterization, the initial crystalline temperature observed here was only 230 °C, which was much lower than that of 575 °C using normal XRD technique after the separated annealing procedure [30]. Nevertheless, it was noticeable that the SAED pattern inserted in Fig. 4(a) still exhibited an amorphous halo, suggesting the presence of a very small amount of nanocrystalline grains precipitated within the amorphous structure at 230 °C. To identify the nanocrystalline features, the corresponding Fast Fourier Transformation (FFT) pattern was carried out for the analysis. As shown in Fig. 4(c), the interplanar spacing of the adjacent lattice fringes was 0.21 nm, closely matching the (103) planes of Cr_2Al [50]. Furthermore, the FFT patterns corresponding to the grain in Fig. 4(d) agreed well with the diffraction patterns of the Cr_2Al phase along $<33\bar{1}>$ zone axis, in which the lattice parameters were calculated to be a = 2.83 Å and c = 4.36 Å, in accordance with the lattice parameters of Cr_2Al (a = 2.79 Å, c = 4.46 Å) rather than Cr_2AlC (a = 2.86 Å, c = 12.82 Å) [33]. These results illustrated the distinct formation of the Cr_2Al solid solution before the presence of the MAX phase, suggesting a possible correlation with the bond energy during phase transformation.

As discussed above, an indication was that the interphase (Cr_2Al) was preferentially generated over the direct formation of the Cr_2AlC MAX phase during *in-situ* heating, in agreement with the previous reports [51]. Previously, Zhou's group [32] synthesized the Cr_2AlC bulks by solid-liquid reaction using Cr, Al, and graphite powders as initial materials, where the appearance of Cr_2Al impurities with (110) and (103) orientations was achieved at 850 °C through XRD measurement. Furthermore, these intermetallic products were substantially transited into the Cr_2AlC phase at 1050 °C. Similar observations were also investigated by Piyush's group [52], in which the Cr_2Al intermetallic compounds acted as the dominant
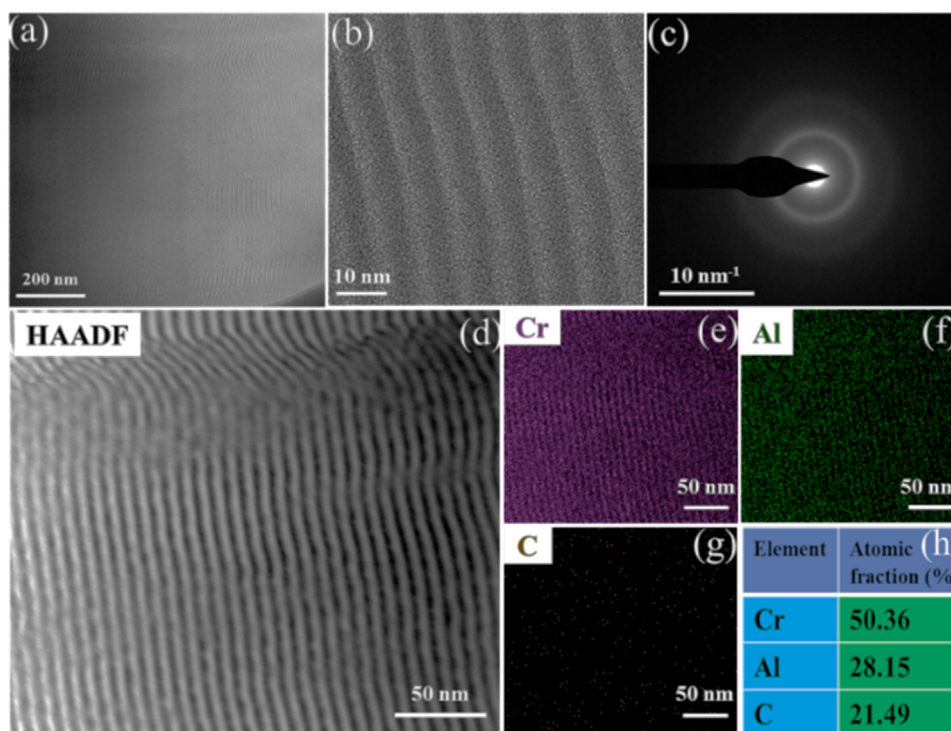
Fig. 2. TEM and EDX mapping images of as-deposited Cr–Al–C coating: (a) TEM bright-field image, (b) HRTEM image, (c) SAED, (d–g) HAADF image and element mapping of Cr, Al, and C, and (h) element atomic fraction.
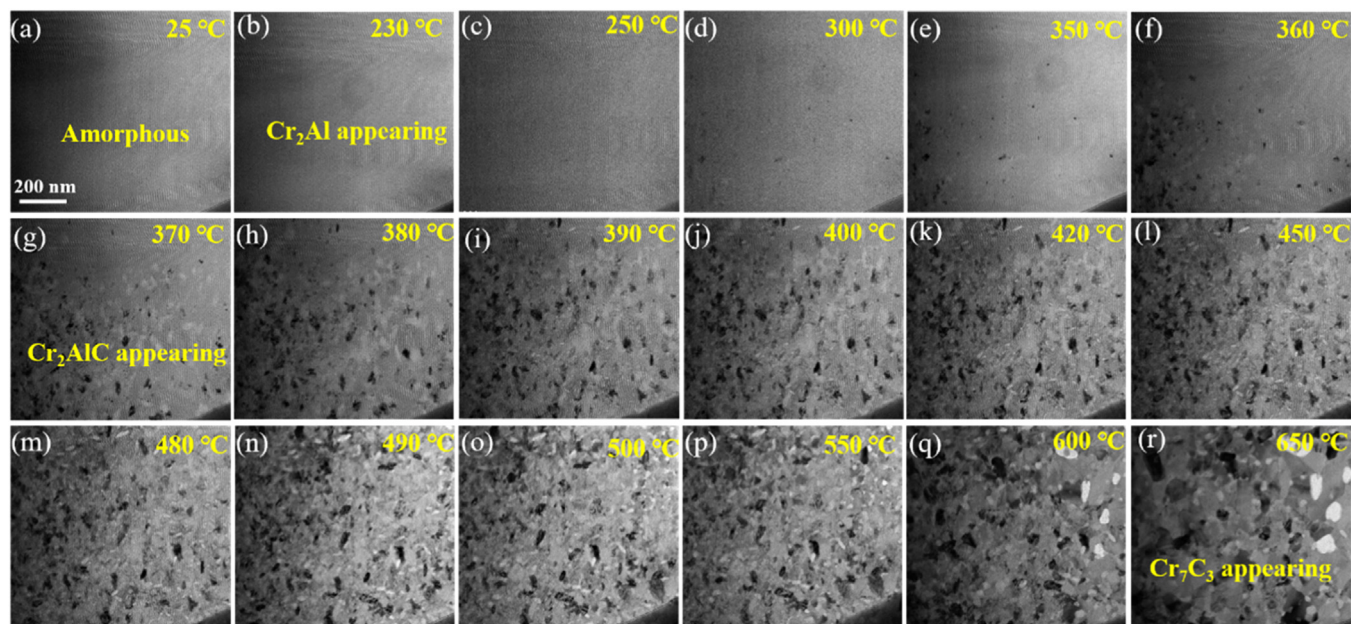

Fig. 3. Microstructure evolution of Cr–Al–C coating during *in-situ* TEM heating. (a–r) the temperature from 25 to 650 °C. All scales were 200 nm same as that in Fig. 3(a).

phase structure at 900 °C, following the existence of the Cr_2AlC MAX phase at a high temperature of 1100 °C. The reasons could be correlated with the kinetic state like activation energy, pre-exponential factor, and reaction mechanism.

Increasing heating temperature led to an increase in the percentage of nanocrystalline grains, accompanied by a gradual diminishment in amorphous characteristics (Fig. 3(c–f)). It was noteworthy that the nanocrystalline grains initially formed at the edge of the specimen before extending to the inside region, which might have arisen from the preparation method for samples. Since the

margin area of the coating sample was directly connected to the heating chip, the sample edge would be overheated than the inside district once the chip was warmed.

Fig. 5 shows the *in-situ* heating TEM image of microstructure characteristics for coatings at the temperature of 370 °C. Compared with the observed structure at 230 °C (Fig. 4), a large number of nanograins were precipitated along with the early generated crystalline grains during heating increment (Fig. 5(a)), indicating the improvement of crystal MAX phase at high temperature. More interestingly, the HRTEM image and corresponding FFT pat-
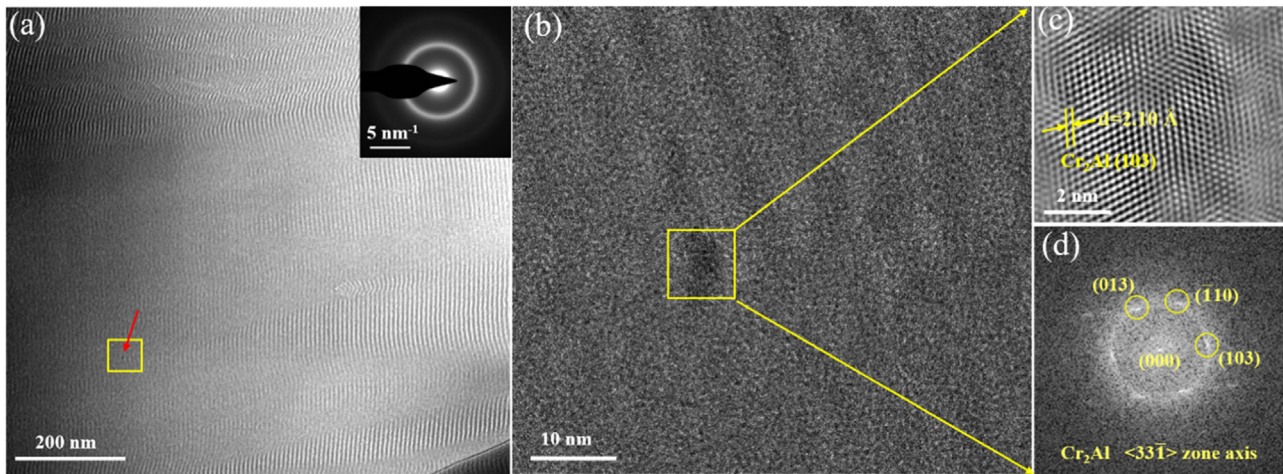
Fig. 4. The samples heated to 230 °C: (a) TEM bright-field image with inserted SAED pattern, (b) HRTEM image from the yellow line framed area in (a), (c) the correspondingly enlarged HRTEM image, and (d) the corresponding FFT pattern from the yellow line framed area in (b).
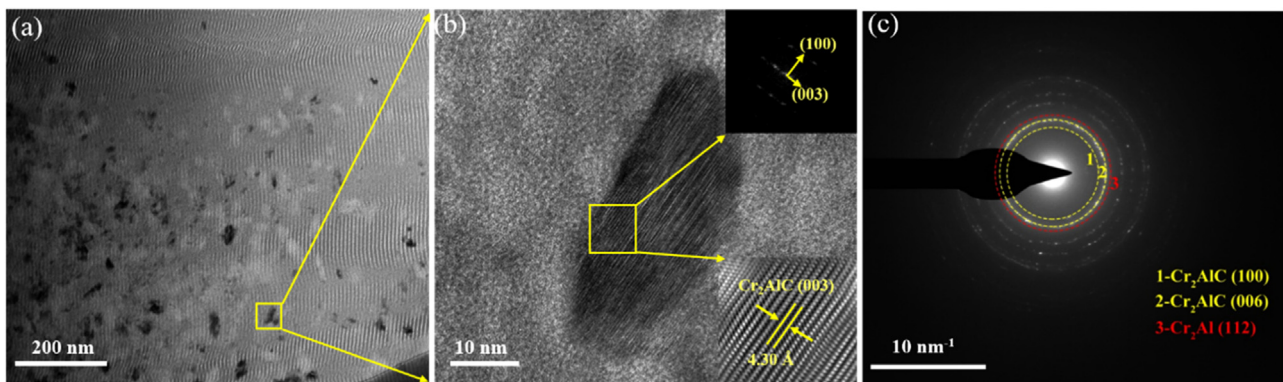
Fig. 5. The coating samples heated at 370 °C: (a) TEM bright-field image and (b) HRTEM image with the inserted corresponding enlarged HRTEM image and FFT pattern from the yellow line framed area, and (c) SAED pattern.

terns clearly identified that these dark contrast grains possessed an interplanar spacing of 0.43 nm between adjacent lattice fringes (Fig. 5(b)), which was well consistent with the interplanar spacing of (003) planes of Cr_2AlC. Noticeable, despite the (100) and (006) planes of the Cr_2AlC phase were distinctly elucidated from the SAED patterns (Fig. 5(c)), corresponding to the lattice parameters with $a = 2.86$ Å and $c = 12.82$ Å [53], there was still a weak diffraction of (112) plane arisen from Cr_2Al phase. This observation revealed the rigid coexistence of both Cr_2AlC and Cr_2Al phases at 370 °C. In general, the Cr_2Al phases were pre-initially nucleated and grew with increments of annealing temperature, and then the Cr_2AlC phases emerged gradually via sufficient reaction between Cr_2Al and pre-introduced C in the coating [51,54]. In this aspect, increasing the temperature to 370 °C was not enough to enable the high transformation from both amorphous and partially intermetallic impurities into MAX phases with complicated crystalline structures that required higher energy to surpass the band barrier.

Further increasing the heating temperature to 500 °C, the density of crystalline nanograins was significantly enhanced, accompanied by a reduced fraction of amorphous structure (Fig. 3(h–o)). Fig. 6 shows the cross-sectional TEM views of coating operated under *in-situ* heating of 500 °C. Evidently, the amorphous nanoscale layered structures seen in the pristine coating virtually vanished, while the high density of crystalline nanograins was generated in the heated coating (Fig. 6(a)). According to the HRTEM image shown in Fig. 6(b), the interplanar spacing of adjacent lattice fringes was about 0.161 and 0.641 nm, fitting perfectly with

the interplanar spacing of (106) and (002) planes of the hexagonal Cr_2AlC phase. It was empirically known that Cr_2AlC owned the HCP crystal structure with a space group of P63/mmc, and the Wyckoff positions for Cr, C, and Al could be assigned to 4f, 2a, and 2d, respectively. Fig. 6(c) presents the STEM-HAADF image with Z-contrast at the atomic scale, viewed from the [100] direction. There was a clearly stacking sequence of the basal planes from the STEM-HAADF image, where the contrast of a certain spot strongly depended on the average atomic numbers of the corresponding atom columns. This observation also evidenced the formation of crystal structure for the Cr_2AlC MAX phase. Furthermore, the calculated lattice parameters a and c, obtained by analyzing the corresponding SAED pattern in Fig. 6(d), were well in accordance with Cr_2AlC reported in our previous studies [55]. Overall, after annealing at the temperature of 500 °C, it was speculated that the pristine Cr–Al–C coating with amorphous matrix was almost transited to the typical nanocrystalline structure of the high-purity Cr_2AlC MAX phase. This *in-situ* information showed the initiative's ability to allow the formation of a high-purity MAX phase at 500 °C, which was approximately 50 °C lower than that synthesized with an *ex-situ* annealing furnace [31]. Additionally, in contrast to the period modulation of elements distributed in the amorphous structure, all the constituent elements of Cr, Al, and C were found to be uniformly embedded within the crystalline Cr_2AlC structure (Fig. 6(e–g)).

It was known that the MAX phase possessed excellent oxidation and hot corrosion resistance as well as outstanding thermal
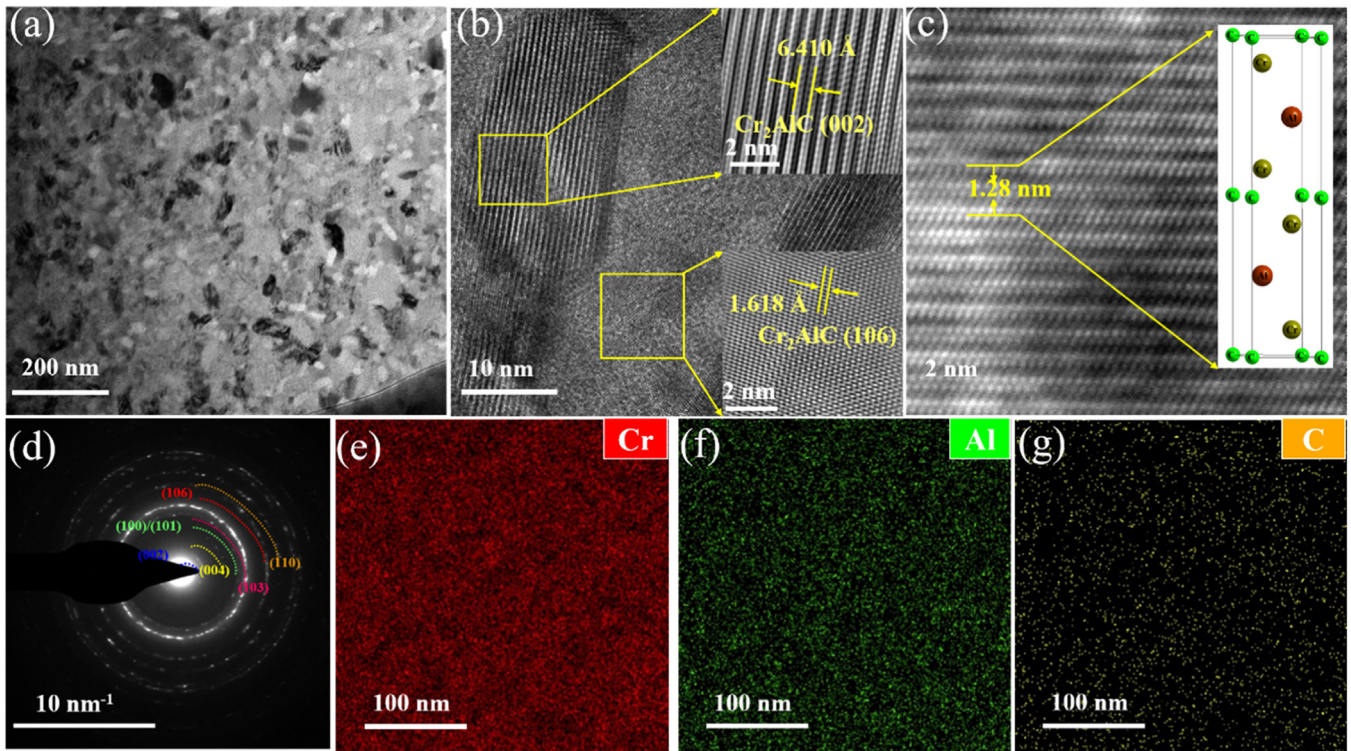
Fig. 6. The coating samples *in-situ* heated to 500 °C: (a) TEM bright-field image, (b) HRTEM image, the insets were the corresponding HRTEM images from the yellow line framed area, (c) high-resolution Z-contrast STEM image, (d) SAED pattern, and (e–g) elemental mapping image of Cr, Al, and C distributed in the heated coating.
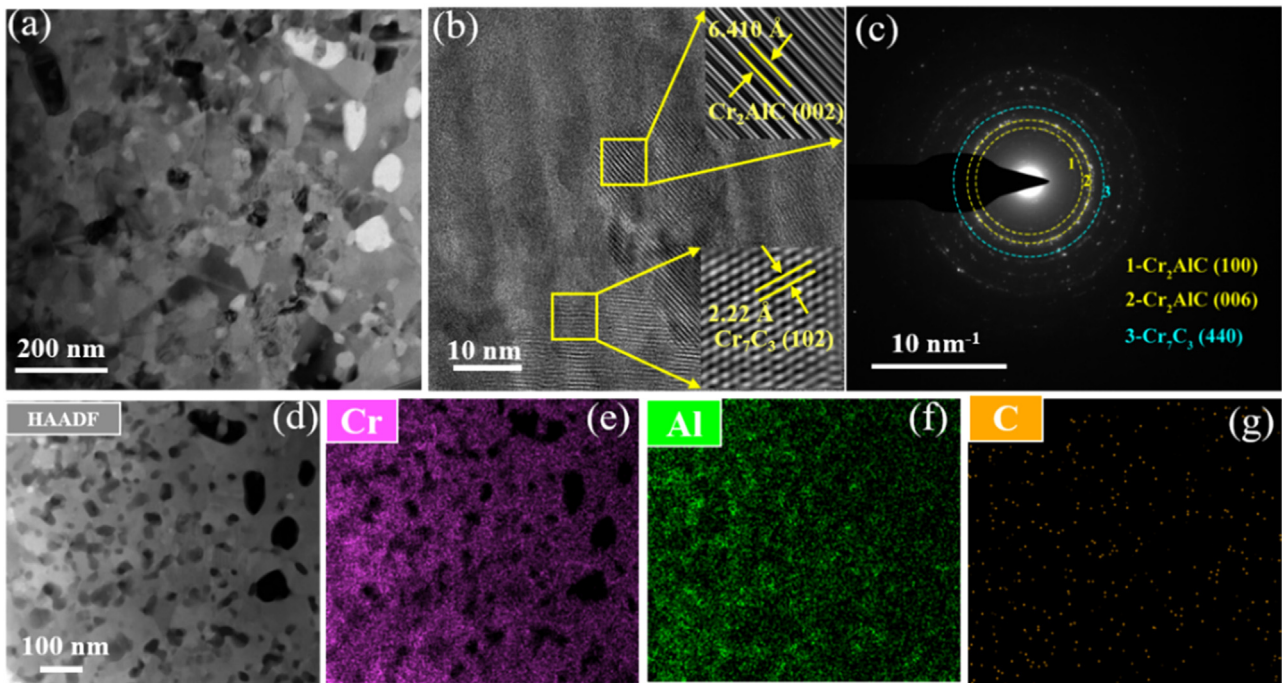
Fig. 7. The coating samples *in-situ* heated to 650 °C: (a) low-magnification bright-field TEM image, (b) HRTEM image, the insets were the corresponding HRTEM images from the yellow line framed area, (c) SAED patterns, and (d–g) HADDF image and element mapping of Cr, Al, and C distributed in coating structure.

stability [56]. Previous literature [24,52] has addressed the superior thermal stability of Cr_2AlC coating maintained up to the temperature of 800 °C. In order to elucidate the structural stability of the Cr_2AlC MAX phase, the coating was further subjected to additional *in-situ* heating (Fig. 3(p–r)). Representatively, Fig. 7 indicates the cross-sectional TEM image and STEM-HAADF image with cor-

responding elemental mapping in the coating at *in-situ* heating of 650 °C. As expected, the larger nanograins were completely illustrated in the structure from the bright field image (Fig. 7(a)) beyond the characteristics originating from the MAX phases. It was noteworthy that although the Cr_2AlC phase dominated the crystalline structure, the newly decomposed Cr_7C_3 crystals were inter-
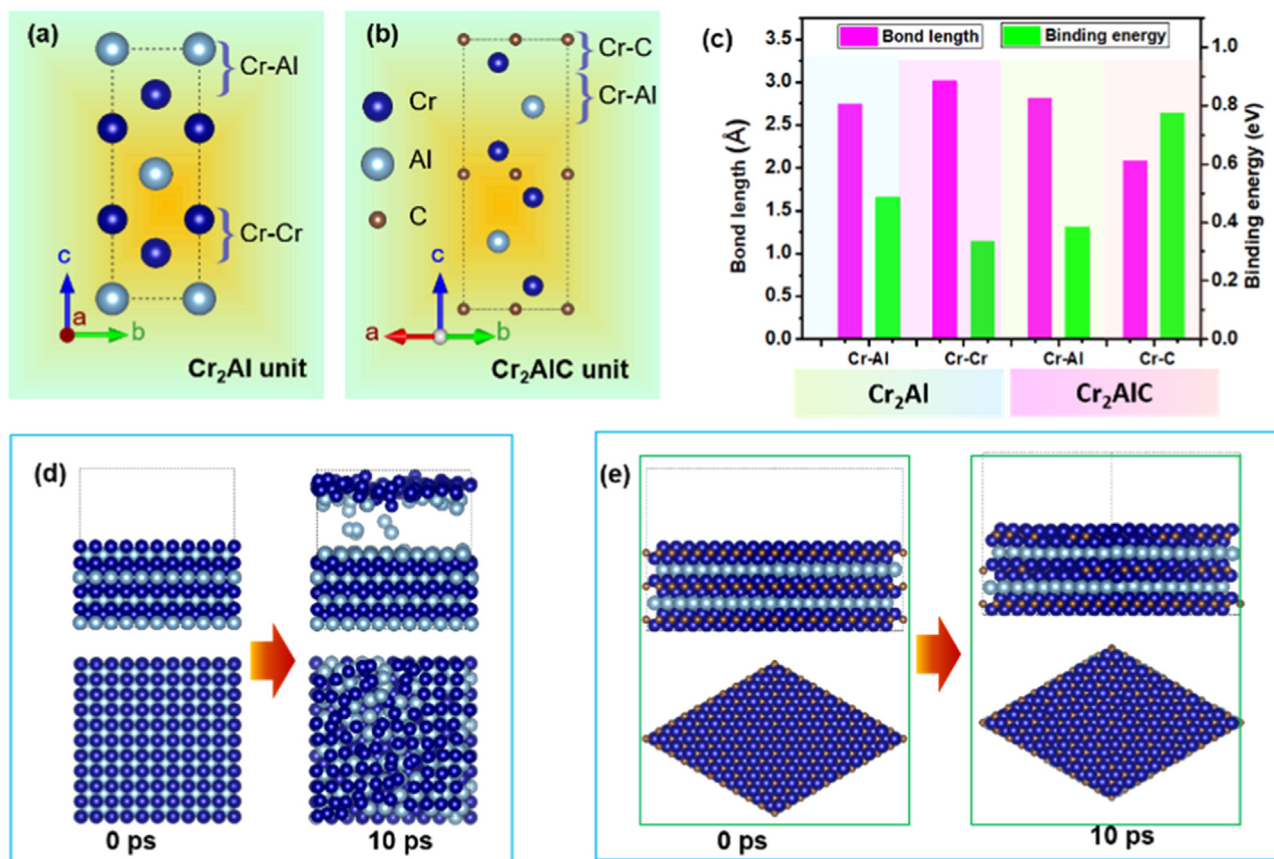
Fig. 8. (a, b) Unit cells of Cr_2Al and Cr_2AlC for simulation. (c) Bond length and binding energy of Cr–Al and Cr–Cr bonds in Cr_2Al, as well as Cr–Al and Cr–C bonds in Cr_2AlC. (d) Ab-initio molecular dynamics simulation of Cr_2Al slab and (e) Cr_2AlC slab in 10 ps at 500 °C.

rupted for viewing (Fig. 7(b, c)). Simultaneously, the distribution of Cr and Al in the structure started to be uneven, as demonstrated in the elemental mapping images (Fig. 7(d–g)). A similar phenomenon was also observed in the crystallization process of amorphous Cr_2AlC [34], where the coating mainly consisted of Cr_7C_3 products and a majority of Cr_2AlC phases above 700 °C. The reasons could be explained from two aspects. Firstly, Al rendered a much larger chemical activity due to the weak bonding of Al–Cr in the Cr_2AlC matrix. Secondly, with the heating at a temperature above 650 °C, the volatility of Al became especially profound, leading to a strong driving for the formation of intermetallic Cr_7C_3 due to the loss of Al atoms. In this regard, it could be proposed that the heating temperature of 500–650 °C would be the optimized key parameter for the fabrication of high-purity Cr_2AlC MAX phase, allowing the wide applications on temperature-sensitive substrates most like titanium alloys and zirconium alloys used for aero-craft engines and nuclear stacks.

Along with the *in-situ* TEM characterizations, we further performed the DFT and AIMD simulations to gain a better atomic-scale understanding of the phase formation and microstructure evolution of Cr_2AlC coatings during the heating process. Fig. 8(a, b) illustrates the established crystal structure for Cr_2Al and Cr_2AlC unit cells, respectively, in which the atomic arrangement along the c-direction revealed a parallel arrangement of Cr, Al, and C atoms. In the case of the Cr_2Al unit, there were specialized one layer of Al atoms and two layers of Cr atoms, with a stacking sequence of Al–Cr–Cr–Al, corresponding to the arrangement involved with Cr–Al and Cr–Cr bonds. On the other hand, Cr_2AlC exhibited a periodic atomic layer arrangement denoted as Al–Cr–C–Cr–Al, particularly including both Cr–Al and Cr–C bonds. Inserting an atomic carbon layer between Cr–Cr in the Cr_2Al unit led to the presence of the

Cr_2AlC unit, adjoint with the disappeared Cr–Cr bonds and the appeared Cr–C bonds. As a result, the stability of Cr_2AlC could be determined by the bond energy of Cr–Cr and Cr–C bonds. Fig. 8(c) indicated the changes in bond lengths and binding energies of Cr–Cr and Cr–Al in Cr_2Al, as well as Cr–Cr and Cr–C in Cr_2AlC for comparison. An obvious informative was that the binding energy of Cr–Al in Cr_2Al (0.486 eV) was higher than that in the Cr_2AlC case (0.385 eV), implying the preferentially formation of Cr_2Al binary intermetallic phase than Cr_2AlC. However, the binding energy of Cr–C in Cr_2AlC was approximately 2.5 times larger than that of Cr–Cr in Cr_2Al. According to the chemical bonding theory, once the provided energy surpassed the binding energy of Cr–Cr but still remained less than that of the Cr–C bond, the Cr–Cr bond could be easily broken, enabling the insertion of carbon atoms to generate the stronger Cr–C bond and thereby facilitating the presence of Cr_2AlC MAX phase. Similar characteristics for various chemical bonds also could be confirmed from the bond length changes (Fig. 8(c)). These results evidenced the observation of *in-situ* TEM characterization discussed above.

Considering the kinetic growth of coating during annealing, Fig. 8(d, e) demonstrates the representative AIMD simulations conducted over a 10 ps period at 500 °C for Cr_2Al and Cr_2AlC units. Details on the simulation process could be visualized in videos 1 and 2 from the supporting information. Increasing the annealing time at 500 °C, there was an obvious view for the broken Cr–Al bonds, together with the distinct existence of intact Cr–C bonds, indicating the appearance of Cr_7C_3 in MAX Cr_2AlC phase. Importantly, this result evidenced that during *in-situ* heating, the evolution of the MAX phase was closely ascribed to the subsequent insertion of C atoms within the predominated Cr_2Al structure, which was quite different from the mechanism of second Al inserting into
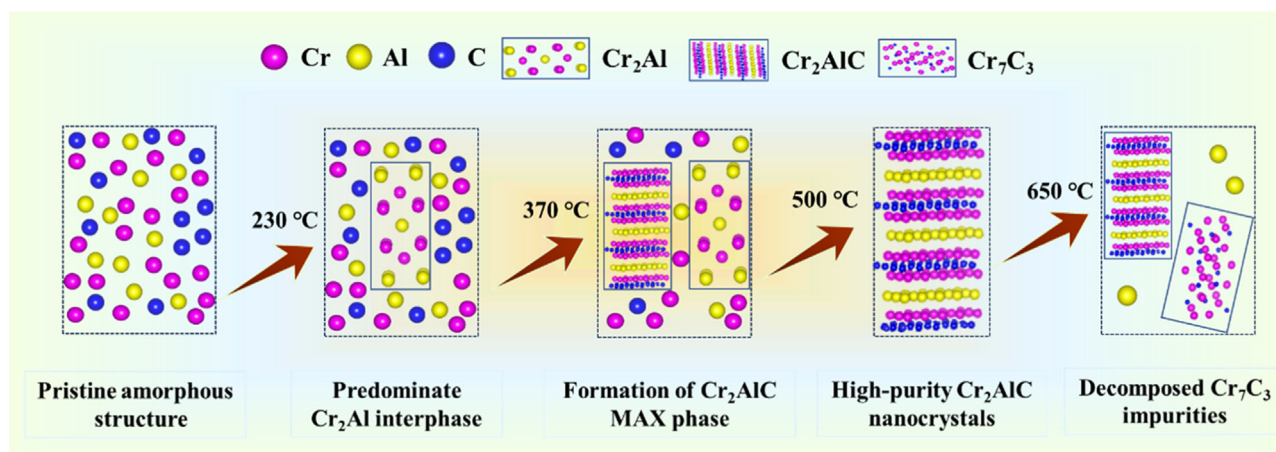
Fig. 9. Schematic diagram of microstructural evolution for Cr_2AlC MAX phase coating involved from as-deposited Cr–Al–C case during the *in-situ* heating process.

the preformed chromium carbide phases for Cr_2AlC [24,29]. Consequently, it could be concluded that the combination of *in-situ* heating TEM characterizations and atomic scale simulations not only revealed the phase formation mechanism of the Cr_2AlC MAX phase but also testified the superior thermal stability of Cr_2AlC coating over Cr_2Al intermetallic impurities under required suitable temperature.

For the easy understating, Fig. 9 shows the schematic diagram of the phase formation mechanism Cr_2AlC MAX phase coating relevant to the dependence of microstructure evolution on *in-situ* heating temperature. Using the cathodic vacuum arc combined with DC magnetron sputtering, the as-deposited Cr–Al–C coating without extra-applied heating displayed the typical amorphous structure, where all the Cr, Al, and C atoms were distributed uniformly within the coating. With increased temperature of 230 °C caused the dominated binary Cr_2Al interphases and followed the small amount of presence of Cr_2AlC nanocrystalline phases at 370 °C, due to the diverse binding energy of Cr–Cr, Cr–Al, and Cr–C bonds. However, the amorphous structure was entirely diminished at 500 °C, accompanied by the predominate observation of high-purity Cr_2AlC MAX phases, which was promoted by the overcoming of the energy barrier for the Cr–C bond. Nevertheless, the overheating energy beyond 650 °C accelerated the decomposition of the Cr_2AlC structure, leading to the existence of Cr_7C_3 impurities and deterioration of the MAX phase without expectation. This microstructural evolution agreed well with the solid state reaction of ternary compounds that generally underwent the three-stage processes [57]. Firstly, the elemental diffusion would be stimulated at interparticle contacts. Secondly, the formation of solid solutions or intermediate phases was strongly determined by the solid solubility. If the generated phases were pretty stable, they would act as an effective diffusion barrier around the unreacted core phases within the unit structure. Finally, the intermediate phases in a transition state could facile react with each other to allow the presence of a stabilized ternary MAX phase.

4. Conclusions

In summary, the Cr–Al–C coatings were initially synthesized at room temperature by using a hybrid deposition technique, which consisted of a cathodic vacuum arc and direct current magnetron sputter plasma sources. Particularly, the focus was elaborated on the microstructural evolution of coatings via *in-situ* heating TEM characterization at 25–650 °C. Furthermore, the theoretical simulations involved the first-principles calculation and Ab-initio molecular dynamic simulation were conducted, in order to identify the

atomic-scaled mechanism for the phase transition during heating. The results showed that the as-deposited Cr–Al–C coating exhibited the typical amorphous structure, with a stoichiometry of Cr:Al:C at approximately 2:1:1. Thanks to the hybrid plasma discharges and substrate rotation, these elements distributed uniformly within the coating but in a distinct layered amorphous feature. Increasing the temperature to 230 °C caused the preferential appearance of binary Cr_2Al interphases, due to the higher binding energy of Cr–Al in Cr_2Al at 0.486 eV than that of 0.385 eV in the Cr_2AlC phase. Subsequently, the surpassing of binding energy yielded a small amount of Cr_2AlC nanocrystalline phase presented under 370 °C heating. Once the heating temperature reached 500 °C, the high-purity nanocrystalline Cr_2AlC MAX phases were distinctly observed, while the amorphous structure and intermetallic impurities were almost completely diminished. The reason behind this observation was that the binding energy of Cr–C in Cr_2AlC was approximately 2.5 times higher than that of the Cr–Cr in Cr_2Al, which substantially promoted the transition of ternary Cr_2AlC phase from binary Cr_2Al intermetallic compounds. When subjected to a temperature of 650 °C, the redundant heating energy resulted in a significant decomposition of Cr_2AlC MAX phases, accompanied by the informative Cr_7C_3 products, which could be evidenced by the preferential broken of Cr–Al bonds over stronger Cr–C bonds in Cr_2AlC structure. The comprehensive observations in the current work not only identify the phase formation mechanism of the Cr_2AlC MAX phase from the initial Cr–Al–C coating with the amorphous structure but also provide the most promising strategy with fundamental insights to tailor the microstructure of MAX phase materials for wide applications that required the combination of excellent oxidation resistance and radiation tolerance as well as the electrical conductivity.

Declaration of competing interest

The authors declare that they have no known competing financial interests or personal relationships that could have appeared to influence the work reported in this paper.

Supplementary materials

Supplementary material associated with this article can be found, in the online version, at doi:10.1016/j.jmst.2024.03.037.

References

[1] M.W. Barsoum, Prog. Solid State Chem. 28 (2000) 201–208.
[2] X. Lei, N.M. Lin, Crit. Rev. Solid State Mater. Sci. 47 (2022) 736–771.
[3] L. Fu, W. Xia, Adv. Eng. Mater. 23 (2021) 2001191.
[4] W.Q. Hu, Z.Y. Huang, Y.B. Wang, X. Li, H.X. Zhai, Y. Zhou, L. Chen, J. Alloys Compd. 856 (2021) 157313.
[5] Z.M. Sun, Int. Mater. Rev. 56 (2013) 143–166.
[6] M.A. Ali, M.M. Hossain, M.M. Uddin, M.A. Hossain, A.K.M.A. Islam, S.H. Naqib, J. Mater. Res. Technol. 11 (2021) 1000–1018.
[7] M.A. Ali, M.M. Hossain, A.K.M.A. Islam, S.H. Naqib, J. Alloys Compd. 857 (2021) 158264.
[8] C. Salvo, E. Chicardi, J. Hernández-Saz, C. Aguilar, P. Gnanaprakasam, R.V. Mangalaraja, Mater. Charact. 171 (2021) 110812.
[9] A. Mussi, A. Henzelmeier, T. Weidner, M. Novelli, Y. Wenbo, F. Cuvilly, T. Grosdidier, A. Guitton, Mater. Charact. 200 (2023) 112882.
[10] Z.C. Li, G.X. Zhou, Z.Y. Wang, J. Yuan, P.L. Ke, A.Y. Wang, J. Eur. Ceram. Soc. 43 (2023) 4673–4683.
[11] Z. Zhang, X.M. Duan, D.C. Jia, Y. Zhou, S.V.D. Zwaag, J. Eur. Ceram. Soc. 41 (2021) 3851–3878.
[12] C. Wang, T. Yang, J. Xiao, S. Liu, J. Xue, Q. Huang, J. Zhang, J. Wang, Y. Wang, R. Koc, J. Am. Ceram. Soc. 99 (2016) 1769–1777.
[13] D.W. Clark, S.J. Zinkle, M.K. Patel, C.M. Parish, Acta Mater. 105 (2016) 130–146.
[14] C. Wang, T. Yang, J. Xiao, S. Liu, J. Xue, J. Wang, Q. Huang, Y. Wang, Acta Mater. 98 (2015) 197–205.
[15] A. Dmitruk, A. Żak, K. Naplocha, W. Dudziński, J. Morgiel, Mater. Charact. 146 (2018) 182–188.
[16] Z.Y. Wang, X.W. Li, W.T. Li, P.L. Kea, A.Y. Wang, Ceram. Int. 45 (2019) 9260–9270.
[17] Z.Y. Wang, G.S. Ma, Z.C. Li, H.T. Ruan, J.H. Yuan, L. Wang, P.L. Ke, A.Y. Wang, Corros. Sci. 192 (2021) 109788.
[18] C.Y. Guo, X.J. Duan, Z. Fang, Y.S. Zhao, T. Yang, E.H. Wang, X.M. Hou, Acta Mater. 241 (2022) 118378.
[19] L. Xiao, S.B. Li, G.M. Song, W.G. Sloof, J. Eur. Ceram. Soc. 31 (2011) 1497–1502.
[20] D.J. Tallman, E.N. Hoffman, E.N. Caspi, B.L. Garcia-Diaz, G. Kohse, R.L. Sindelar, M.W. Barsoum, Acta Mater. 85 (2015) 132–143.
[21] C. Wang, T. Yang, S. Kong, J. Xiao, J. Xue, Q. Wang, C. Hu, Q. Huang, Y. Wang, J. Nucl. Mater. 440 (2013) 606–611.
[22] X. Shi, M. Wang, W. Zhai, Z. Xu, Q. Zhang, Y. Chen, Mater. Des. 45 (2013) 179–189.
[23] C. Magnus, D. Cooper, L. Ma, W.M. Rainforth, Wear 448–449 (2020) 203169.
[24] J.H. Yuan, Z.Y. Wang, G.S. Ma, X.J. Bai, Y. Li, X. Cheng, P.L. Ke, A.Y. Wang, J. Mater. Sci. Technol. 143 (2023) 140–152.
[25] Z.J. Lin, M.S. Li, J.Y. Wang, Y.C. Zhou, Acta Mater. 55 (2007) 6182–6191.
[26] M. Ougier, A. Michau, F. Lomello, F. Schuster, H. Maskrot, M.L. Schlegel, J. Nucl. Mater. 528 (2020) 151855.
[27] V.D. Jovic, B.M. Jovic, S. Gupta, T.E. Raghy, M.W. Barsoum, Corros. Sci. 48 (2006) 4274–4282.
[28] G.S. Ma, D. Zhang, P. Guo, H. Li, Y. Xin, Z.Y. Wang, A.Y. Wang, J. Mater. Sci. Technol. 105 (2022) 36–44.
[29] J.H. Yuan, S.H. Zhou, H.C. Wu, Z.Y. Wang, Y. Zhang, G.X. Zhou, G.S. Ma, P.L. Ke, A.Y. Wang, Scr. Mater. 235 (2023) 115594.
[30] Z.R. Zhang, Y.H. Qian, J.J. Xu, J. Zuo, M.S. Li, Corros. Sci. 178 (2021) 109062.
[31] G.S. Ma, J.H. Yuan, R.D. Chen, H. Li, H. Wu, J.S. Yan, Z.Y. Wang, A.Y. Wang, Appl. Surf. Sci. 597 (2022) 153670.
[32] Z. Lin, Y. Zhou, M. Li, J. Wang, Z. Metallkd. 96 (2005) 291–296.
[33] A. Abdulkadhim, M. Baben, T. Takahashi, V. Schnabel, M. Hans, C. Polzer, P. Polcik, J.M. Schneider, Surf. Coat. Technol. 206 (2011) 599–603.
[34] J.J. Li, Y.H. Qian, D. Niu, M.M. Zhang, Z.M. Liu, M.S. Li, Appl. Surf. Sci. 263 (2012) 457–464.
[35] B. Stelzer, X. Chen, P. Bliem, M. Hans, B. Volker, R. Sahu, C. Scheu, D. Primetzhofer, J.M. Schneider, Sci. Rep. 9 (2019) 8266.
[36] M. Rath, B. Friessnegger, P. Angerer, P. Raninger, A. Stanojevic, E. Kozeschnik, Mater. Charact. 206 (2023) 113382.
[37] J. Nutter, J. Qi, H. Farahani, W.M. Rainforth, S.V.D. Zwaag, Acta Mater. 252 (2023) 118924.
[38] S. Kikuchi, M. Tezura, M. Kimura, N. Yamaguchi, S. Kitaoka, T. Kizuka, Scr. Mater. 150 (2018) 50–53.
[39] Y.P. Ivanov, C.M. Meylan, N.T. Panagiotopoulos, K. Georgarakis, A.L. Greer, Acta Mater. 196 (2020) 52–60.
[40] G. Kresse, J. Furthmüller, Phys. Rev. B 54 (1996) 11169.
[41] J.P. Perdew, K. Burke, M. Ernzerhof, Phys. Rev. Lett. 77 (1996) 3865.
[42] G. Kresse, D. Joubert, Phys. Rev. B 59 (1999) 1758.
[43] A. Abbad, W. Benstaali, H.A. Bentounes, S. Bentata, Y. Benmalem, Solid State Commun. 228 (2016) 36–42.
[44] Y.G. Wang, Y. Yoon, V.A. Glezakou, J. Am. Chem. Soc. 135 (2013) 10673–10683.
[45] C. Zhu, S. Kais, X.C. Zeng, J.S. Francisco, I. Gladich, J. Am. Chem. Soc. 139 (2017) 27–30.
[46] T.W. Zhou, M. Wang, Z.G. Zang, L. Fang, Adv. Energy Mater. 9 (2019) 1900664.
[47] I. Muhammad, U. Younis, W. Wu, H. Xie, A. Khaliq, Q. Sun, J. Power Sources 480 (2020) 228876.
[48] L.A. Truflandier, J. Autschbach, J. Am. Chem. Soc. 132 (2010) 3472–3483.
[49] Z.Y. Wang, W. Li, Y. Liu, J. Shuai, P.L. Ke, A.Y. Wang, Appl. Surf. Sci. 502 (2020) 144130.
[50] R. Mertens, Z. Sun, D. Music, J.M. Schneider, Adv. Eng. Mater. 6 (2004) 903–907.
[51] W.B. Tian, P.L. Wang, Y.M. Kan, G.J. Zhang, Y.X. Li, D.S. Yan, Mater. Sci. Eng. A 443 (2007) 229–234.
[52] P. Sharma, O.P. Pandey, J. Therm. Anal. Calorim. 143 (2020) 3997–4008.
[53] J.J. Li, L.F. Hu, F.Z. Li, M.S. Li, Y.C. Zhou, Surf. Coat. Technol. 204 (2010) 3838–3845.
[54] E.I. Zamulaeva, E.A. Levashov, E.A. Skryleva, T.A. Sviridova, P.V. Kiryukhantsev-Korneev, Surf. Coat. Technol. 298 (2016) 15–23.
[55] Z.Y. Wang, G.S. Ma, L.L. Liu, L. Wang, P.L. Ke, Q. Xue, A.Y. Wang, Corros. Sci. 167 (2020) 108492.
[56] X. Duan, Z. Fang, T. Yang, C. Guo, Z. Han, D. Sarker, X. Hou, E. Wang, J. Adv. Ceram. 11 (2022) 1307–1318.
[57] R. Yembadi, B.B. Panigrahi, Adv. Powder Technol. 28 (2017) 732–739.